



# MANTA: A Large-Scale Multi-View and Visual-Text Anomaly Detection Dataset for Tiny Objects

Lei Fan<sup>1\* \*</sup>  
Donglin Di<sup>4</sup>

Dongdong Fan<sup>2</sup>  
Kai Yi<sup>5</sup>

Zhiguang Hu<sup>3</sup>  
Maurice Pagnucco<sup>1</sup>

Yiwen Ding<sup>2</sup>  
Yang Song<sup>1</sup>

<sup>1</sup>UNSW Sydney

<sup>2</sup>Gaozhe

<sup>3</sup>SCAU

<sup>4</sup>Li Auto

<sup>5</sup>University of Cambridge

<https://grainnet.github.io/MANTA>

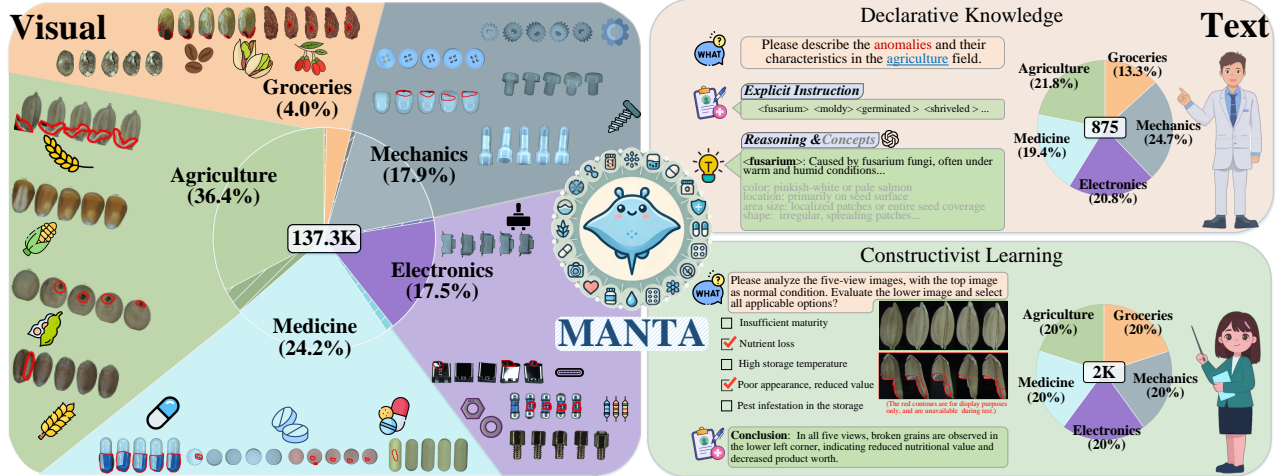


Figure 1. **Overview of MANTA.** It consists of both visual and text components. The visual part includes over 137K multi-view images spanning five domains. The text part is divided into two subsets: *Declarative Knowledge*, comprising 875 words describing common anomalies, and *Constructivist Learning*, which includes 2K Image-text multiple-choice questions.

## Abstract

We present *MANTA*, a visual-text anomaly detection dataset for tiny objects. The visual component comprises over 137.3K images across 38 object categories spanning five typical domains, of which 8.6K images are labeled as anomalous with pixel-level annotations. Each image is captured from five distinct viewpoints to ensure comprehensive object coverage. The text component consists of two subsets: *Declarative Knowledge*, including 875 words that describe common anomalies across various domains and specific categories, with detailed explanations for *what, why, how*, including causes and visual characteristics; and *Constructivist Learning*, providing 2K multiple-choice questions with varying levels of difficulty, each paired with images and corresponded answer explanations. We also propose a baseline for visual-text tasks and conduct extensive benchmarking experiments to evaluate advanced methods across different settings, highlighting the challenges and efficacy of our dataset.

\*Corresponding author: lei.fan1@unsw.edu.au

## 1. Introduction

Anomaly detection (AD) has gained significant attention across various fields [12, 15, 30, 43, 46, 47]. High-quality datasets, e.g., MVTec [5], play a crucial role in advancing AD models and establishing unified benchmarks. These datasets are predominantly designed for industrial objects of large physical sizes and typically rely on single-view cameras to capture individual images, where anomalies are often more discernible and easier to detect.

In real-world applications, particularly those involving natural objects and manufactured items, there is a substantial volume of samples with tiny physical sizes [32]. Unlike larger objects that can be readily inspected [49], identifying anomalies in these tiny objects requires considerable labor and cost, making it a critical yet underexplored area. For example, inspecting medical pills, agricultural seeds, or mechanical components presents unique challenges. Traditional single-view imaging setups [30] often fail to capture critical perspectives due to inherent design limitations, resulting in incomplete visual information. Compared to larger objects with clear textures and structural characteristics [18], tiny objects require high concentration during data

collection and inspection.

In this paper, we present **MANTA**, a **M**ulti-view **A**nomaly detection with **T**ext Analysis dataset for tiny objects, as illustrated in Figure 1. We acquired a large number of tiny objects from common domains in daily life and industrial environments, and designed a prototype equipped with five high-resolution cameras to capture visual data from five different angles, ensuring comprehensive surface coverage for each object. We then provide high-quality data with detailed annotations for both visual and textual components. Specifically, the visual component comprises over 137.3K multi-view images, including over 8K images annotated as anomalies with pixel-level annotations. Each multi-view image captures five viewpoints of a single tiny object. These images cover 38 categories, *e.g.*, wheat kernels, medical tablets, Type-C interfaces, and screws, grouped into five typical domains: agriculture, medicine, electronics, mechanics, and groceries.

The text component consists of two subsets: Declarative Knowledge (*DeclK*) and Constructivist Learning (*ConsL*). Specifically, *DeclK* summarizes expert domain knowledge through text descriptions at three levels including explicit instruction, reasoning and concepts corresponding to  $\langle \textit{what}, \textit{why}, \textit{how} \rangle$ . We provide 875 instruction words covering both domain-specific and category-specific anomalies across five domains. Each instruction is represented by a noun or adjective to describe types of anomalies (*e.g.*, scratches); reasoning explains the cause of the anomaly (*e.g.*, physical impact); and concepts outline common visual characteristics of the anomaly, *e.g.*, typical colors like white and gray, locations often found on the surface, irregular sizes, and common shapes appearing as lines. *ConsL* is designed to emulate a human learning approach through visual comparisons and corresponding multiple-choice questions (MCQ), reflecting the process of human learning by analyzing images and selecting answers based on visual cues. We provide over 2000 MCQs with varying levels of difficulty, each consisting of a pair of normal-normal or normal-anomaly images, accompanied by five domain-specific options, answers, and explanations.

We also propose a baseline by fine-tuning a pretrained multimodal language-image model [26] to perform our *ConsL* task. Furthermore, we conduct extensive experiments to evaluate advanced methods on our dataset under various settings, *e.g.*, one-for-one, multi-class, and text prompt learning. Our contributions are listed as follows:

- We release a large-scale visual-text AD dataset: MANTA. It contains over 137K multi-view images of tiny objects spanning 38 categories across five domains.
- MANTA includes two text subsets: *DeclK*, summarizing expert knowledge for various anomalies at three levels, and *ConsL*, providing multiple-choice questions paired with images and explanations.

- We propose a baseline model by fine-tuning foundation model to perform visual-language tasks on *ConsL*.
- We conduct comprehensive benchmarking experiments, involving over 400 evaluations across five different settings on our dataset, demonstrating the challenges and efficacy of MANTA.

## 2. Related Work

### 2.1. Anomaly Detection Datasets

Early studies [9, 13, 21, 23, 34, 35, 48] focused on specific domains and provided limited categories for visual discrimination of structural defects. Datasets like MVTEC AD [5], VisA [61] and MVTEC LOCO AD [6] introduce a diverse range of objects and textures for standard benchmarks. Although these datasets offer high-quality images and annotations, they are constrained to single-view setups and lack standardized backgrounds. MVTEC 3D [7] and Real3d-ad [29] provide point cloud data acquired by 3D sensors, but are constrained by limited sample volumes. Recently, RealIAD [53] contains diverse objects with multi-view images, though full-surface inspection requires manual intervention.

In contrast to these studies, which rely on single-view or incomplete multi-view setups, we provided a dataset for tiny objects captured from five views, ensuring comprehensive coverage of their full surfaces.

### 2.2. Anomaly Detection Settings

Visual anomaly detection task is typically formulated as an unsupervised manner [37], where only normal samples are available for model training. Existing studies can be broadly categorized into reconstruction-based [11, 31, 40], synthesis-based [25, 33, 56, 59], embedding-based [10, 44], and memory-based methods [4, 42]. These methods effectively transform the unsupervised setting into a supervised one by constructing pretext tasks or learning compact representations of normal samples. Unlike these studies, some studies focused on developing ‘one-for-all’ models [14, 16, 55] capable of handling multiple categories simultaneously. Recently, several studies [20, 22, 27, 28, 45, 60] explored text prompts, such as defect names, to leverage the capabilities of foundation models like CLIP [39].

In addition to the above settings, MANTA’s multi-view setup supports both view-level and object-level AD evaluations. Moreover, two text subsets cover domain knowledge and multiple-choice questions, facilitating comprehensive analysis of visual-language models.

## 3. MANTA

We begin with data acquisition, including data collection, data-capturing prototype, and preprocessing procedure. Next, we introduce MANTA, detailing its visual and textual components and the relevant challenges.

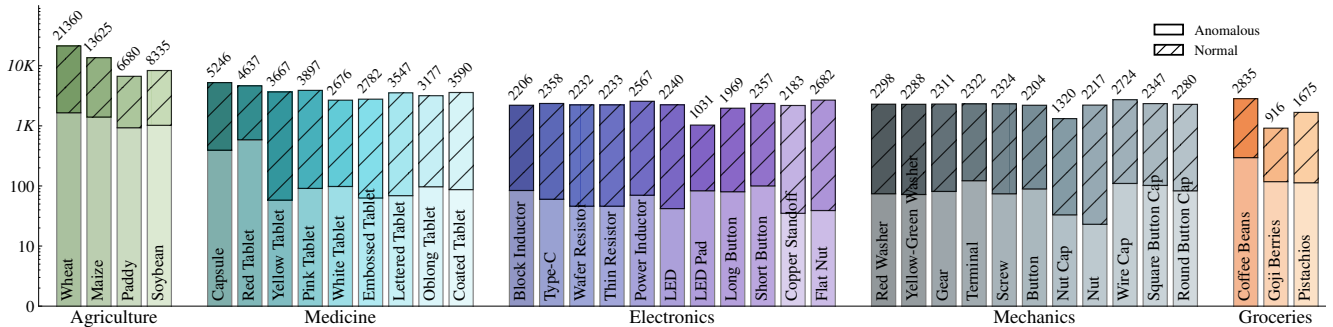


Figure 2. **The data distribution of the visual component in MANTA.** It contains 137,338 multi-view images across 38 categories from five typical domains: Agriculture, medicine, electronics, mechanics, and groceries. Each histogram represents a category, with different color groups indicating domains. For better visualization, a  $\log_{10}$  scale is used on the y-axis.

### 3.1. Data Acquisition

**Sample Collection.** We gathered and curated a large-scale repository comprising over 300K tiny objects across various domains including agriculture, pharmaceuticals, industry, food, to daily items. The physical sizes of these objects mainly range from  $4^3$  to  $20^3 mm^3$ . We preprocessed and filtered approximately 200K objects for subsequent data construction. To ensure data balance and increase the number of anomalous samples, we manually introduced a series of controlled defects. Detailed information regarding object categories and physical size can be found in the *Supp.*

**Prototype.** We constructed a prototype equipped with five high-resolution cameras to capture the surface information of tiny objects individually, as shown in Figure 3. The tiny object is placed on a transparent plate, with four cameras arranged in a quadrilateral formation, tilted downward at  $30^\circ$ , and one additional camera positioned vertically beneath, pointing upward. Given the small size of tiny objects, achieving high-quality, low-noise images is crucial. To ensure this, shadowless light sources are placed on both sides, providing consistent and uniform illumination. This setup captures five-view images for each object, where each camera operates at 1170 DPI (the bottom one operates at 1250 DPI), ensuring high-quality images capable of detecting defects as small as  $0.2^3 mm^3$ .

### 3.2. Image Annotations and Statistics

**Preprocessing and Annotations.** The raw image from each camera has a resolution of  $1272 \times 1016$ . We used a mechanical setup to separate tiny objects individually. After capturing visual information, we applied basic morphological operations to coarsely localize the object’s center, followed by cropping to a fixed size to ensure consistent scaling across similar objects while preserving relative size information. Background artifacts were removed manually, and image quality was calibrated using a standardized color plate to enhance uniformity and consistency across

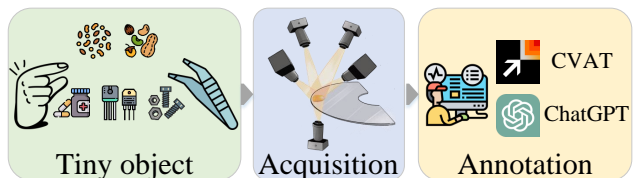


Figure 3. **Data acquisition.** We collected tiny objects from various domains, constructed a prototype to capture visual information, and annotated them using CVAT and ChatGPT.

the dataset. For each object, the five processed images were aligned and vertically merged into a single five-view composite image based on the same camera order.

We recruited a team of four expert inspectors to classify images into normal or anomalous categories, with pixel-level annotations highlighting the anomalous regions using CVAT [52]. Additionally, two lightweight classification [17] and segmentation models [41] were trained to filter out low-quality or annotation errors through a progressive hold-out process. All results were then manually re-validated to ensure accuracy and consistency.

Table 1. Comparison with various AD datasets. *#Cate* and *#O/Poly* refer to the number of object categories and labeled polygons per object respectively. The *object* row indicates that each sample represents multiple views of a single object.

Datasets(‘ year)	Sample Statistics			Attributes		Annotations	
	#Norm	#Anom	#Tota	#Cate	View	#O/Poly	Modal
BTAD’21 [35]	952	290	1,242	3	Single	2.6	☒
MPDD’21 [23]	1,064	282	1,346	6	Single	1.8	☒
MVTec AD’21 [5]	4,096	1,258	5,354	15	Single	1.5	☒
VISA’22 [61]	9,621	1,200	10,821	12	Single	3.5	☒
LOCO-AD’22 [6]	2,347	993	5,354	5	Single	1.2	☒
GoodsAD’24 [57]	4,464	1,659	6,123	6	Single	1.1	☒
Read-IAD’24 [53]	99,721	51,329	151,050		Single		
Read-IAD ( <i>object</i> )	14,568	15,642	30,210	30	Multi	3.7	☒
MANTA ( <i>single</i> )	652,455	34,235	686,690		Single		
MANTA ( <i>object</i> )	128,721	8,617	137,338	38	Multi	5.1	☒ ☒

**Data Statistics.** The visual component in MANTA contains 137,338 multi-view images. It includes 38 categories spanning five typical domains, as shown in Figure 2. The ontology and examples can be found in the *Supp.* All images are in RGB format, with resolutions ranging from  $162 \times 705$  to  $1117 \times 3365$  pixels. Among these, 8,617 images are categorized as anomalous and include mask annotations to highlight the anomalous regions. Considering the imbalance between normal and anomalous data, for each category with  $N$  anomalous images, we partitioned the training and testing sets by randomly selecting  $2N$  normal images along with all anomalous images to form the test set, while the remaining normal data was used for the training set. Compared to existing AD datasets, as shown in Table 1, MANTA leads significantly in both dataset size, category, and annotation volume. Notably, similar to the multi-view Real-IAD dataset, we report both *single-view* (each view treated as a separate sample) and *object-view* (multi-view images of an object treated as a single sample) information. Additionally, we further provide text descriptions in the following section. Additionally, we provide text descriptions in the subsequent section.

**Challenges.** Unlike existing datasets that primarily focus on industrial products [5, 53, 61], our dataset presents heterogeneity, pose-agnostic and size-sensitive challenges due to the unique characteristics of tiny objects, as illustrated in Figure 4. Specifically, *heterogeneity* refers to the inherent variability observed within normal samples of the same category, as our dataset includes tiny natural products, e.g., wheat and soybean kernels, which naturally differ in shape, color, and texture due to growth conditions. *Pose-agnostic* implies that the viewing angles for the same object are agnostic, with precise pose alignment not guaranteed, as controlling the orientation of certain tiny objects is highly complex and costly. *Size-sensitive* highlights the critical importance of size variations for specific objects, especially in fields such as medicine and mechanics, where even minor deviations in size can directly affect dosage accuracy and

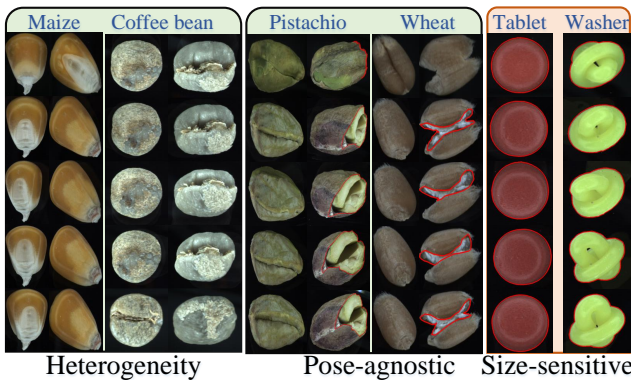


Figure 4. Examples illustrating the image data challenges.

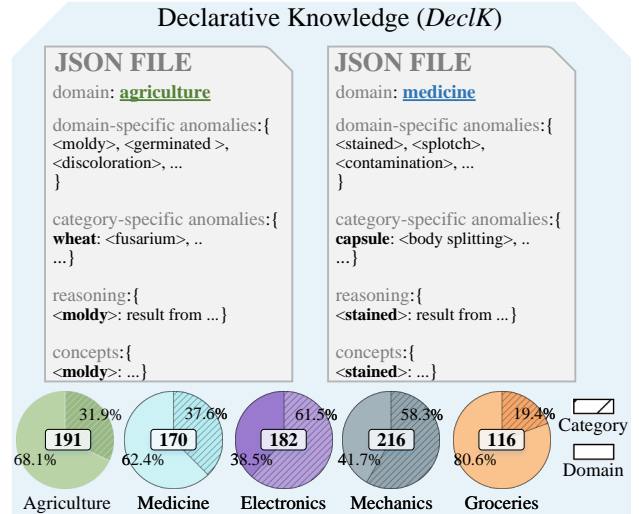


Figure 5. Format and data distribution of Declarative Knowledge.

assembly specifications.

### 3.3. Text Annotations and Statistics

To advance the applicability of anomaly detection datasets in visual-language tasks [1, 26, 39], we identified and summarized two common forms of text annotations. First, domain experts often provide detailed descriptions of common anomalies within their field, supplementing specific categories with additional information; we refer to this as **declarative knowledge**. Second, experts typically use comparative illustrations with normal-normal or normal-anomaly images and pose key questions to guide learning; we refer to this method as **constructivist learning**.

**Declarative Knowledge (DeclK).** It leverages expert knowledge to produce comprehensive textual descriptions, structured across three levels: explicit instruction, reasoning and concepts corresponding to *<what, why, how>*, as depicted in Figure 1. The motivation is to align with cognitive load theory [3], supporting learners who excel in verbal-linguistic intelligence by providing language-based pathways for understanding.

Specifically, experts codified a specialized vocabulary (noun or adjective) to describe *explicit instruction* for both domain-specific and category-specific anomalies. For example, in the agriculture domain, “moldy” represents a domain-specific anomaly, while “wheat blight” is a category-specific anomaly for wheat. These terms are further supplemented with detailed explanations of underlying causes, providing *reasoning* and progression of anomalies. To enhance the understanding of *concepts*, anomalies are described through their corresponding visual attributes, e.g., color, shape, texture and size. Both *reasoning* and *concepts* annotations are enriched with insights generated by large

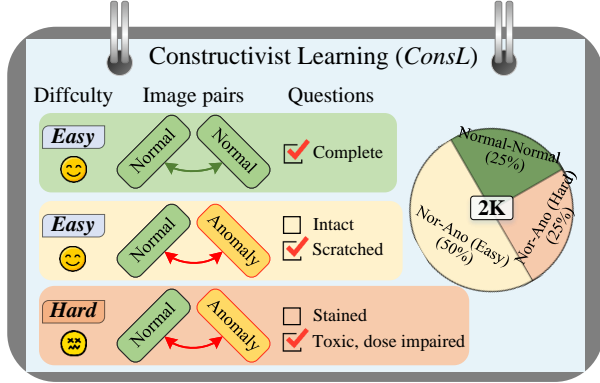


Figure 6. **Overview of Constructivist Learning.** We provide 2K MCQs with both easy and hard difficulty levels, each containing five options and explanations.

language models (ChatGPT-4).

We constructed 875 *explicit instructions* for all domains including 391 category-specific words, with corresponding *reasoning* and *concepts* provided in JSON format, as shown in Figure 5. All text descriptions and generated descriptions underwent thorough review to ensure accuracy. *DeclK* serves as a structured representation bridging textual and visual domains by creating a detailed textual resource, enhancing the detection and reasoning capabilities of models in visual-language tasks.

**Constructivist Learning (ConsL).** Inspired by learning theory [36] and recent multimodal studies [50, 51], we developed *ConsL* which involves creating pair-wise images and formulating corresponding multiple-choice questions (MCQ) based on category-specific anomaly information. The motivation is rooted in dual coding theory, which posits that learners achieve better understanding when information is presented in both visual and verbal formats, actively engaging them in identifying and differentiating defects.

Specifically, we manually constructed an average of over 400 pairs of images and corresponding MCQ within each domain, as shown in Figure 6. The image pairs consist of both normal-normal and normal-anomalous pairs, with MCQ settings focused on highly relevant and concerned anomalies. Each MCQ is provided with five options and a prompt instructs “select the correct answer based on the image pair of <category name>”. For normal-anomalous pairs, we additionally provide a conclusion describing the anomalies in terms of spatial location, shape, size and type. *ConsL* requires the model to identify whether an anomaly exists, describe it, and provide reasoning for its decision. It introduces a structured framework for visual comparison and reasoning, facilitating learning through comparative analysis with text-based questions.

**Challenges.** Both text data components represent distinct learning approaches, each suited to different cognitive

strategies. *DeclK* provides a hierarchical summary of domain knowledge, explaining anomalies from the perspectives of <what, why, how>. However, these descriptions are general depictions of anomalies and are not directly tied to specific images. In contrast, *ConsL* presents pairwise images with specialized questions, focusing on practical anomaly identification without detailed annotations or pre-defined categories. Both *DeclK* and *ConsL* require strong capabilities from models, aiming to enhance conceptual comprehension and facilitate visual-text reasoning.

## 4. Baseline

For the *ConsL* subset, we explore the application of existing Visual Question Answering and visual-text frameworks [2, 39], and fine-tuned a model based on BLIP-2 [26] model with LoRA [19].

**Architecture.** We followed the BLIP-2 [26] architecture, as illustrated in Figure 7. The model comprises three main modules: an image encoder, a querying transformer, and an LLM. Specifically, the image encoder is a pre-trained Vision Transformer used to extract features from input images. The querying transformer consists of two transformer modules that interact with visual features and decode textual output using cross-attention layers, capturing text-related features from visual features and text prompts and thereby bridging the visual and language modality. The LLM includes a pretrained large language model (OPT) [58] used for generating language output.

**Fine-tuning.** Both the visual ViT and language OPT models are pretrained on extensive data, so we fix their parameters to reduce computational cost and mitigate catastrophic forgetting of pretrained knowledge. We employ LoRA [19] for efficient fine-tuning by using low-rank decomposition matrices.

For each MCQ in *ConsL*, given two images  $I_1$  and  $I_2$  along with a set of options  $\langle Q_1, \dots, Q_5 \rangle$ , we vertically con-

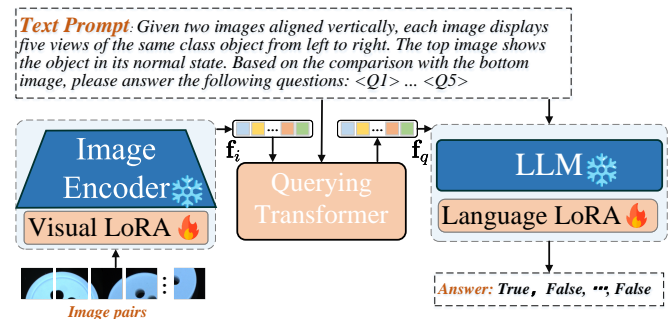


Figure 7. **Overview of our baseline for ConsL.** It consists of an image encoder with a visual LoRA (to extract image features), a Querying Transformer (to bridge the modality gap), and LLM with a language LoRA (for output generation), based on BLIP-2 [26].

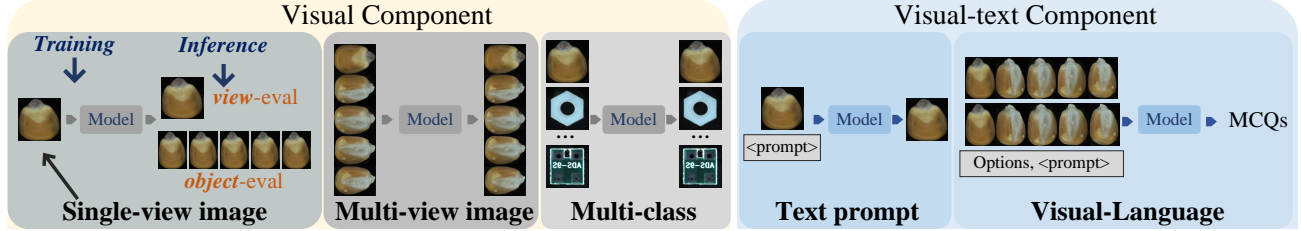


Figure 8. **Evaluation settings.** As MANTA includes both visual and textural components, with each image having five views, we established five settings according to their training inputs: *Single-view* uses a single view as input for each category; *Multi-view* utilizes all five views of an object for each category; *Multi-class* combines single-view inputs from different categories train a single model; *Text prompt* leverages a single view with text prompts for training; and *Visual-Language* takes a pair of images and prompts to perform MCQ tasks.

concatenate the two images and pass them through an image projector to extract image embeddings, which are then fed into the visual ViT to obtain visual features  $\mathbf{f}_i$ . We employ cross-entropy loss to classify the input images:

$$L_{ce} = - \sum_{i=1}^B c_i \log(\hat{c}_i), \quad (1)$$

where  $B$  denotes the batch size,  $c_i$  represents the true class label (e.g., button object), and  $\hat{c}_i$  is the predicted class from the input images  $[I_1, I_2]$ .

We further construct a prompt  $p_t$  based on given options  $\langle Q_1, \dots, Q_5 \rangle$ , which is tokenized to produce the corresponding text features  $\mathbf{f}_t$ . The visual features  $\mathbf{f}_i$  and  $\mathbf{f}_t$  are concatenated and fed into the querying transformer to extract the query features  $\mathbf{f}_q$ . Finally,  $\mathbf{f}_q$  and  $\mathbf{f}_t$  are combined  $[\mathbf{f}_q, \mathbf{f}_t]$  and sent to the language module, which is fine-tuned to produce the final output based on the autoregressive loss.

## 5. Experiments

### 5.1. Settings and Details

**Evaluation Settings.** We established five evaluation settings based on different inputs and training approaches, as shown in Figure 8. We first conducted experiments on the visual component to explore advanced methods under both one-for-one (training a single model for each class) and multi-class settings (training a single model for multiple classes). Next, we evaluated the combined visual and textual setup, focusing on few-shot evaluation settings with text prompt learning and visual-language models.

**Metrics and Implementation Details.** We reported standard image-level (I-) and pixel-level (P-) Area Under the Receiver Operating Characteristics (AUROC) scores [37, 42, 56] to evaluate model performance in anomaly detection and localization. Complete details on model implementation, additional metrics, and comprehensive experimental results are provided in the *Supp.*

### 5.2. Results on Visual Component

**The single-view setting.** Considering that existing methods are typically trained using single-view data, including other multi-view datasets (e.g., Real-IAD [53]), we evaluated single-view data and conducted nearly 200 experiments to compare several advanced methods: RD [11], DMAD [31], PatchCore [42], CDO [8], and SimpleNet [33]. Results were reported using two evaluation strategies: *view-eval*, where each view is treated as an individual test sample, and *object-eval* where five views of an object are considered a single test sample.

As shown in Table 2, all models achieved performance below 97% of I-AUROC across all domains, with the agriculture and groceries averaging below 90% of I-AUROC. This highlights the challenging nature of our dataset compared to other datasets (e.g., MVTEC [5]) with 100% of I-AUROC, as the heterogeneity and pose-agnostic challenges in our data require models to effectively capture complex normal patterns. Additionally, we observed that reconstruction-based models performed relatively worse compared to other approaches. We attribute this to the fact that many anomalous samples in tiny objects possess large anomalous regions, which reconstruction-based methods often struggle to address effectively.

We observed that performance for *view-eval* and *object-eval* are similar. *view-eval* is computed separately for each individual view, while *object-eval* aggregates five views of an object before calculation. This grouping effectively averages out variations in model performance across different views, leading to a more stable overall evaluation.

**The multi-view setting.** We conducted over 150 experiments using five-view images of an object as individual training samples, with results reported at the *object-eval* level. Since the size of multi-view inputs is five times larger than single-view images, we adapted several advanced methods, including RD [11], Patchcore [42], CDO [8], and DMAD [31], to accommodate this configuration due to memory constraints.

As shown in Table 3, all models demonstrated promising

Table 2. **Comparisons of single-view setting for each class.** Models are trained using single-view images and reported results in both *view-eval* and *object-eval* (predictions from five views of an object). All results are presented as I-/P-AUROC (%). We reported only the average results across multiple classes for each domain, with details provided in the *Supp.*

Model(*year)	Agriculture		Medicine		Electronics		Mechanics		Groceries		Average	
	<i>view-eval</i>	<i>object-eval</i>										
RD'22 [11]	84.7/85.2	87.2/85.3	86.4/94.0	92.3/94.1	86.6/93.5	89.2/93.4	81.0/91.9	85.7/91.8	71.2/85.3	73.5/85.3	82.0/90.0	85.6/90.0
PatchCore'22 [42]	93.0/93.0	94.2/93.0	96.5/96.7	97.4/97.0	97.1/98.8	97.0/98.8	95.8/98.7	96.4/98.7	86.2/91.5	90.8/91.5	93.7/95.7	95.2/95.8
CDO'23 [8]	90.0/90.6	91.3/90.4	95.2/95.4	95.2/95.5	94.1/98.6	91.9/98.6	91.1/98.4	90.3/98.4	85.4/90.4	87.7/89.3	91.2/94.7	91.3/94.4
DMAD'23 [31]	84.5/84.9	86.9/85.2	84.6/93.3	91.2/91.2	87.4/92.1	90.1/92.2	80.2/90.3	85.3/90.4	75.1/87.5	77.0/87.4	82.6/89.6	86.1/89.7
SimpleNet'23 [33]	86.3/83.3	91.2/84.3	91.1/87.2	94.7/88.3	89.6/90.3	92.5/91.2	86.4/88.7	89.6/88.5	82.2/82.5	86.5/84.9	87.1/86.4	90.9/87.5

performance across the five domains, with an average of I-AUROC of 91% and P-AUROC of 94%. Compared to *single-view* inputs, we attribute this improved performance to the *multi-view* images providing multiple perspectives that share critical features of the object. However, considering the computational cost of using multi-view inputs, our subsequent experiments primarily focused on *single-view* data.

**The multi-class setting.** We also evaluated the popular multi-class setting, where all classes within each domain are mixed for the single-view training. We evaluated recent methods, including UniAD [55], CRAD [24] and HGAD [54], as shown in Table 4. These models exhibited performance below I-AUROC of 90% and P-AUROC of 91% across the five domains, representing a decline compared to the *single-view* and *multi-view* settings. We attribute this to the variability among objects, even within the same domain. For example, in the agriculture domain, wheat and maize exhibit notable differences, while in electronics, the appearances of Type-C connectors and LEDs differ significantly. This variability imposes high demands on multi-class models to generalize and learn normal patterns across different classes simultaneously.

### 5.3. Results on Text Component

As MANTA includes two text subsets: *DeclK* and *ConsL*, we explored two types of visual-text settings: **Text prompt**, which uses text prompts from *DeclK* combined with images to train a model for anomaly detection; and **Visual-Language**, which leverages images, options, and conclusions from *ConsL* to fine-tune our baseline model.

**The text-prompt setting.** We explored our *DeclK* subset using advanced text prompt AD methods, including

Table 3. **Comparisons of multi-view setting for each class.** Models are trained using multi-view images. We presented only the averaged results (I-/P-AUROC, %) across multiple classes for each domain, with details provided in the *Supp.*

Model	Agriculture	Medicine	Electronics	Mechanics	Groceries	Average
RD'22 [11]	86.9/89.5	94.3/96.1	94.9/98.5	96.1/98.7	81.1/87.3	90.6/94.0
PatchCore'22 [42]	94.1/93.0	96.8/96.2	96.8/98.7	96.6/98.6	91.0/91.8	95.0/95.7
CDO'23 [8]	90.7/90.4	95.4/95.5	92.3/98.6	91.3/98.4	87.8/89.5	91.5/94.5
DMAD'23 [31]	88.5/89.7	95.1/95.8	94.2/98.3	93.3/98.3	80.0/86.3	90.2/93.7

Table 4. **Comparisons of multi-class setting.** Models are trained using single-view mixed data across all categories within each domain. Results are presented as I-/P-AUROC (%).

Model(*year)	Agriculture	Medicine	Electronics	Mechanics	Groceries	Average
UniAD'23 [55]	70.5/81.9	91.3/93.3	93.6/97.7	90.2/97.2	66.7/76.8	82.4/89.4
CRAD'24 [24]	85.2/86.4	94.2/94.6	94.5/96.5	92.9/96.9	76.1/83.5	88.6/91.6
HGAD'24 [54]	85.5/88.6	92.6/93.7	91.0/94.3	83.5/94.8	74.8/71.7	85.5/88.6

WinCLIP [22], PromptAD [27] and VCP-CLIP[38]. Due to computational resource constraints, we focused on one-shot learning and constructed a small-scale test set of 1000 images, with equal numbers of normal and anomalous samples per domain. For the text prompt, we randomly selected explicit instructions from *DeclK* (formatted as “*<instruction>* of *<category>*”) along with visual concepts as negative samples, while we randomly sampled other explicit instructions, using the format “without *<instruction>*” as positive samples.

As shown in Figure 9, the three methods achieved moderate performance under the one-shot learning setting, with WinCLIP surpassing an average of 75% in I-AUROC and 90% in P-AUROC across five domains. This indicates that our *DeclK* subset can serve as effective supervision, bridging the gap to extract visual-text features from foundation models [39], enhancing anomaly detection capabilities.

**The visual-language setting.** We evaluated our base-

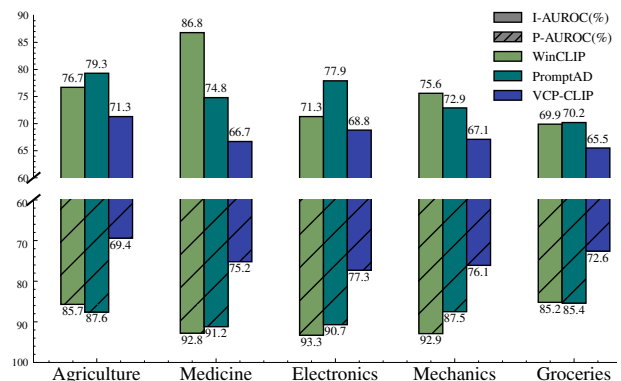


Figure 9. **Comparison of text prompt setting in one-shot learning.** Models are trained using text data from *DeclK*.

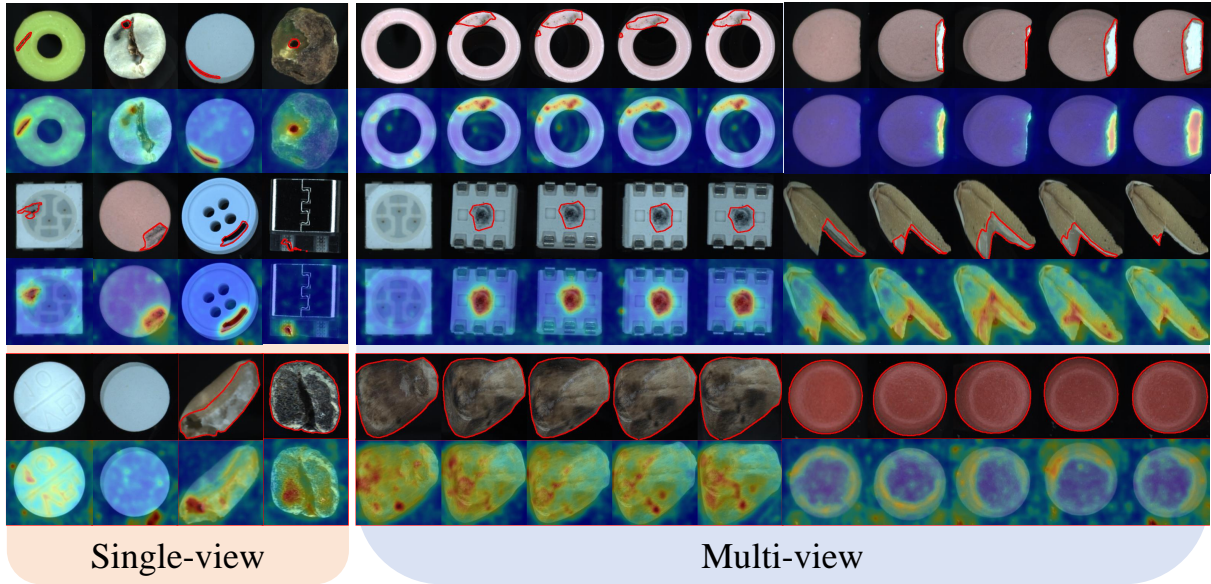


Figure 10. **Visualization of single-view and multi-view.** We presented both successful and failure cases to qualitatively illustrate the challenges posed by our MANTA dataset.

line model on *ConsL* in both zero-shot and few-shot learning. We randomly selected 50% of the data from each domain with balanced difficulty levels for training, while the remaining 50% was used for testing. We reported two metrics: *option* accuracy, where each option is scored individually, and *question* accuracy, where an entire MCQ is considered correct only if all options are correctly answered. We vertically concatenated two images and provided the text prompt: “Given two images aligned vertically, each image displays five views of the same class object from left to right. The top image shows the object in its normal state. Based on the comparison with the bottom image, please answer the following questions:  $\langle Q1 \rangle, \dots, \langle Q5 \rangle$ ..”.

As shown in Table 5, compared to the zero-shot learning, the model using few-shot learning achieved an average of 50.2% and 5.7% in *option* and *question* accuracy respectively, but still exhibited unsatisfactory performance. We attribute this to the domain gap between our images and the pretrained data of the baseline’s visual ViT. Additionally, in terms of *question* accuracy, especially for hard MCQs, the models need to accurately identify anomalies and infer the

Table 5. **Performance of visual-language setting.** Our baselines are tested in zero-shot and one-shot settings. Results are presented as *option/question* (%) accuracy. N-A(hard) denotes Normal-Anomaly image pairs with a hard level of difficulty.

Settings	N-N(easy)	N-A(easy)	N-A(hard)	Average
zero-shot	44.8/3.5	51.8/2.5	38.7/1.5	45.1/2.5
few-shot	<b>53.8/6.9</b>	<b>62.0 /5.5</b>	<b>50.7/4.6</b>	<b>55.2/5.7</b>

correct options based on the nature of the anomaly and the object’s category, which demands strong visual understanding and reasoning capabilities.

#### 5.4. Visualization

We presented qualitative results for the single-view and multi-view settings, as illustrated in Figure 10. In the *single-view* setting, the model effectively localized smaller anomalous regions, such as insect-attacked holes, and mold spots on grains. However, larger anomalies often led to missed areas, such as complete impurities or larger broken regions. In the *multi-view* setting, the model demonstrated good detection of small anomalous regions and maintained consistency across multiple views. However, due to the larger image size, more localization errors were observed.

#### 6. Conclusion

In this paper, we introduce MANTA, a comprehensive visual-text anomaly detection dataset for tiny objects spanning five domains. With over 137K multi-view images and two text subsets, our dataset presents unique challenges and diverse settings for anomaly detection. Extensive experiments highlighted the complexities of MANTA, paving the way for advancements in visual-language applications.

**Limitations.** MANTA focuses on tiny objects, which presents significant differences compared to other conventional objects. Although we utilized five cameras, certain areas may remain partially uncovered (*e.g.*, hexagonal sides). Furthermore, due to cost constraints, the size of our text data subset is limited.

## References

- [1] Jean-Baptiste Alayrac, Jeff Donahue, Pauline Luc, et al. Flamingo: a visual language model for few-shot learning. *NeurIPS*, 35:23716–23736, 2022. 4
- [2] Stanislaw Antol, Aishwarya Agrawal, Jiasen Lu, et al. Vqa: Visual question answering. In *ICCV*, pages 2425–2433, 2015. 5
- [3] Krzysztof R Apt, Howard A Blair, and Adrian Walker. Towards a theory of declarative knowledge. In *Foundations of deductive databases and logic programming*, pages 89–148. Elsevier, 1988. 4
- [4] Jaehyeok Bae, Jae-Han Lee, and Seyun Kim. Pni: Industrial anomaly detection using position and neighborhood information. In *ICCV*, pages 6373–6383, 2023. 2
- [5] Paul Bergmann, Michael Fauser, David Sattlegger, and Carsten Steger. Mvtec ad—a comprehensive real-world dataset for unsupervised anomaly detection. In *CVPR*, pages 9592–9600, 2019. 1, 2, 3, 4, 6
- [6] Paul Bergmann, Kilian Batzner, Michael Fauser, David Sattlegger, and Carsten Steger. Beyond dents and scratches: Logical constraints in unsupervised anomaly detection and localization. *IJCV*, 130(4):947–969, 2022. 2, 3
- [7] Paul Bergmann., Xin Jin., David Sattlegger., and Carsten Steger. The mvtec 3d-ad dataset for unsupervised 3d anomaly detection and localization. In *International Joint Conference on Computer Vision*, pages 202–213, 2022. 2
- [8] Yunkang Cao, Xiaohao Xu, Zhaoge Liu, and Weiming Shen. Collaborative discrepancy optimization for reliable image anomaly localization. *IEEE Transactions on Industrial Informatics*, 19(11):10674–10683, 2023. 6, 7
- [9] Diego Carrera, Fabio Manganini, Giacomo Boracchi, and Ettore Lanzarone. Defect detection in sem images of nanofibrous materials. *IEEE Transactions on Industrial Informatics*, 13(2):551–561, 2016. 2
- [10] Thomas Defard, Aleksandr Setkov, Angélique Loesch, and Romaric Audigier. Padim: a patch distribution modeling framework for anomaly detection and localization. In *ICPR*, pages 475–489. Springer, 2021. 2
- [11] Hanqiu Deng and Xingyu Li. Anomaly detection via reverse distillation from one-class embedding. In *CVPR*, pages 9737–9746, 2022. 2, 6, 7
- [12] Lei Fan, Yiwen Ding, Dongdong Fan, Donglin Di, Maurice Pagnucco, and Yang Song. Grainspace: A large-scale dataset for fine-grained and domain-adaptive recognition of cereal grains. In *CVPR*, pages 21116–21125, 2022. 1
- [13] Lei Fan, Yiwen Ding, Dongdong Fan, Yong Wu, Maurice Pagnucco, and Yang Song. Identifying the defective: Detecting damaged grains for cereal appearance inspection. In *ECAI*, pages 660–667. IOS Press, 2023. 2
- [14] Hwei Guo, Liping Ren, Jingjing Fu, et al. Template-guided hierarchical feature restoration for anomaly detection. In *ICCV*, pages 6447–6458, 2023. 2
- [15] Songqiao Han, Xiyang Hu, Hailiang Huang, Minqi Jiang, and Yue Zhao. Adbench: Anomaly detection benchmark. *NeurIPS*, 35:32142–32159, 2022. 1
- [16] Haoyang He, Jiangning Zhang, et al. A diffusion-based framework for multi-class anomaly detection. In *AAAI*, pages 8472–8480, 2024. 2
- [17] Kaiming He, Xiangyu Zhang, Shaoqing Ren, and Jian Sun. Deep residual learning for image recognition. In *CVPR*, pages 770–778, 2016. 3
- [18] Hadi Hojjati, Thi Kieu Khanh Ho, and Naregs Armanfard. Self-supervised anomaly detection in computer vision and beyond: A survey and outlook. *Neural Networks*, page 106106, 2024. 1
- [19] Edward J Hu, Phillip Wallis, Zeyuan Allen-Zhu, Yuanzhi Li, Shean Wang, Lu Wang, Weizhu Chen, et al. Lora: Low-rank adaptation of large language models. In *ICLR*. 5
- [20] Chaoqin Huang, Aofan Jiang, Jinghao Feng, Ya Zhang, Xinchao Wang, and Yanfeng Wang. Adapting visual-language models for generalizable anomaly detection in medical images. In *CVPR*, pages 11375–11385, 2024. 2
- [21] Yibin Huang, Congying Qiu, and Kui Yuan. Surface defect saliency of magnetic tile. *The Visual Computer*, 36(1):85–96, 2020. 2
- [22] Jongheon Jeong, Yang Zou, Taewan Kim, et al. Winclip: Zero-/few-shot anomaly classification and segmentation. In *CVPR*, pages 19606–19616, 2023. 2, 7
- [23] Stepan Jezek, Martin Jonak, Radim Burget, Pavel Dvorak, and Milos Skotak. Deep learning-based defect detection of metal parts: evaluating current methods in complex conditions. In *International Congress on Ultra Modern Telecommunications and Control Systems and Workshops*, pages 66–71, 2021. 2, 3
- [24] Joo Chan Lee, Taejune Kim, Eunbyung Park, Simon S. Woo, and Jong Hwan Ko. Continuous memory representation for anomaly detection. *ECCV*, 2024. 7
- [25] Chun-Liang Li, Kihyuk Sohn, Jinsung Yoon, et al. Cutpaste: Self-supervised learning for anomaly detection and localization. In *CVPR*, pages 9664–9674, 2021. 2
- [26] Junnan Li, Dongxu Li, Silvio Savarese, and Steven Hoi. Blip-2: Bootstrapping language-image pre-training with frozen image encoders and large language models. In *ICML*, pages 19730–19742. PMLR, 2023. 2, 4, 5
- [27] Xiaofan Li, Zhizhong Zhang, Xin Tan, Chengwei Chen, Yanyun Qu, Yuan Xie, and Lizhuang Ma. Promptad: Learning prompts with only normal samples for few-shot anomaly detection. In *CVPR*, pages 16838–16848, 2024. 2, 7
- [28] Jiaqi Liu, Kai Wu, et al. Unsupervised continual anomaly detection with contrastively-learned prompt. In *AAAI*, pages 3639–3647, 2024. 2
- [29] Jiaqi Liu, Guoyang Xie, Ruitao Chen, et al. Real3d-ad: A dataset of point cloud anomaly detection. *NeurIPS*, 36, 2024. 2
- [30] Jiaqi Liu, Guoyang Xie, Jinbao Wang, et al. Deep industrial image anomaly detection: A survey. *Machine Intelligence Research*, 21(1):104–135, 2024. 1
- [31] Wenrui Liu, Hong Chang, Bingpeng Ma, Shiguang Shan, and Xilin Chen. Diversity-measurable anomaly detection. In *CVPR*, pages 12147–12156, 2023. 2, 6, 7
- [32] Yang Liu, Peng Sun, Nickolas Wergeles, and Yi Shang. A survey and performance evaluation of deep learning methods

- for small object detection. *Expert Systems with Applications*, 172:114602, 2021. 1
- [33] Zhikang Liu, Yiming Zhou, Yuansheng Xu, and Zilei Wang. Simplenet: A simple network for image anomaly detection and localization. In *CVPR*, pages 20402–20411, 2023. 2, 6, 7
- [34] Domingo Mery, Vladimir Rizzo, Uwe Zscherpel, German Mondragón, Iván Lillo, Irene Zuccar, Hans Lobel, and Miguel Carrasco. Gdxyray: The database of x-ray images for nondestructive testing. *Journal of Nondestructive Evaluation*, 34(4):42, 2015. 2
- [35] Pankaj Mishra, Riccardo Verk, Daniele Fornasier, Claudio Piciarelli, and Gian Luca Foresti. Vt-adl: A vision transformer network for image anomaly detection and localization. In *International Symposium on Industrial Electronics*, pages 01–06, 2021. 2, 3
- [36] A Sullivan Palincsar. Social constructivist perspectives on teaching and learning. *Annual review of psychology*, 49(1): 345–375, 1998. 5
- [37] Guansong Pang, Chunhua Shen, Longbing Cao, and Anton Van Den Hengel. Deep learning for anomaly detection: A review. *ACM computing surveys (CSUR)*, 54(2):1–38, 2021. 2, 6
- [38] Zhen Qu, Xian Tao, Mukesh Prasad, Fei Shen, Zhengtao Zhang, Xinyi Gong, and Guiguang Ding. Vcp-clip: A visual context prompting model for zero-shot anomaly segmentation. *ECCV*, 2024. 7
- [39] Alec Radford, Jong Wook Kim, Chris Hallacy, et al. Learning transferable visual models from natural language supervision. In *ICML*, pages 8748–8763. PMLR, 2021. 2, 4, 5, 7
- [40] Nicolae-Cătălin Ristea, Neelu Madan, Radu Tudor Ionescu, Kamal Nasrollahi, Fahad Shahbaz Khan, Thomas B Moeslund, and Mubarak Shah. Self-supervised predictive convolutional attentive block for anomaly detection. In *CVPR*, pages 13576–13586, 2022. 2
- [41] Olaf Ronneberger, Philipp Fischer, and Thomas Brox. U-net: Convolutional networks for biomedical image segmentation. In *MICCAI*, pages 234–241, 2015. 3
- [42] Karsten Roth, Latha Pemula, Joaquin Zepeda, Bernhard Schölkopf, Thomas Brox, and Peter Gehler. Towards total recall in industrial anomaly detection. In *CVPR*, pages 14318–14328, 2022. 2, 6, 7
- [43] Karsten Roth, Latha Pemula, Joaquin Zepeda, Bernhard Schölkopf, Thomas Brox, and Peter Gehler. Towards total recall in industrial anomaly detection. In *CVPR*, pages 14318–14328, 2022. 1
- [44] Lukas Ruff, Robert Vandermeulen, Nico Goernitz, Lucas Deecke, Shoaib Ahmed Siddiqui, Alexander Binder, Emmanuel Müller, and Marius Kloft. Deep one-class classification. In *ICML*, pages 4393–4402. PMLR, 2018. 2
- [45] Fumiaki Sato, Ryo Hachiuma, and Taiki Sekii. Prompt-guided zero-shot anomaly action recognition using pre-trained deep skeleton features. In *CVPR*, pages 6471–6480, 2023. 2
- [46] Sebastian Schmidl, Phillip Wenig, and Thorsten Papenbrock. Anomaly detection in time series: a comprehensive evaluation. *Proceedings of the VLDB Endowment*, 15(9):1779–1797, 2022. 1
- [47] Hongjun Su, Zhaoyue Wu, Huihui Zhang, and Qian Du. Hyperspectral anomaly detection: A survey. *IEEE Geoscience and Remote Sensing Magazine*, 10(1):64–90, 2021. 1
- [48] Domen Tabernik, Samo Šela, Jure Skvarč, and Danijel Skočaj. Segmentation-based deep-learning approach for surface-defect detection. *Journal of Intelligent Manufacturing*, 31(3):759–776, 2020. 2
- [49] Kang Tong and Yiquan Wu. Deep learning-based detection from the perspective of small or tiny objects: A survey. *Image and Vision Computing*, 123:104471, 2022. 1
- [50] Shengbang Tong, Erik Jones, and Jacob Steinhardt. Mass-producing failures of multimodal systems with language models. *NeurIPS*, 36, 2024. 5
- [51] Shengbang Tong, Zhuang Liu, Yuexiang Zhai, Yi Ma, Yann LeCun, and Saining Xie. Eyes wide shut? exploring the visual shortcomings of multimodal llms. In *CVPR*, pages 9568–9578, 2024. 5
- [52] VAT.ai Corporation. Computer Vision Annotation Tool (CVAT), 2024. 3
- [53] Chengjie Wang, Wenbing Zhu, Bin-Bin Gao, Zhenye Gan, Jiangning Zhang, Zhihao Gu, Shuguang Qian, Mingang Chen, and Lizhuang Ma. Real-iad: A real-world multi-view dataset for benchmarking versatile industrial anomaly detection. In *CVPR*, pages 22883–22892, 2024. 2, 3, 4, 6
- [54] Xincheng Yao, Ruoqi Li, Zefeng Qian, Lu Wang, and Chongyang Zhang. Hierarchical gaussian mixture normalizing flows modeling for unified anomaly detection. In *ECCV*, 2024. 7
- [55] Zhiyuan You, Lei Cui, Yujun Shen, Kai Yang, Xin Lu, Yu Zheng, and Xinyi Le. A unified model for multi-class anomaly detection. *NeurIPS*, 35:4571–4584, 2022. 2, 7
- [56] Vitjan Zavrtanik, Matej Kristan, and Danijel Skočaj. Draem—a discriminatively trained reconstruction embedding for surface anomaly detection. In *ICCV*, pages 8330–8339, 2021. 2, 6
- [57] Jian Zhang, Runwei Ding, Miaoju Ban, and Linhui Dai. Pku-goodsad: A supermarket goods dataset for unsupervised anomaly detection and segmentation. *IEEE Robotics and Automation Letters*, 2024. 3
- [58] Susan Zhang, Stephen Roller, Naman Goyal, Mikel Artetxe, Moya Chen, Shuohui Chen, Christopher Dewan, Mona Diab, Xian Li, Xi Victoria Lin, et al. Opt: Open pre-trained transformer language models. *arXiv preprint arXiv:2205.01068*, 2022. 5
- [59] Ximiao Zhang, Min Xu, and Xiuzhuang Zhou. Realnet: A feature selection network with realistic synthetic anomaly for anomaly detection. In *CVPR*, pages 16699–16708, 2024. 2
- [60] Jiawen Zhu and Guansong Pang. Toward generalist anomaly detection via in-context residual learning with few-shot sample prompts. In *CVPR*, pages 17826–17836, 2024. 2
- [61] Yang Zou, Jongheon Jeong, Latha Pemula, Dongqing Zhang, and Onkar Dabeer. Spot-the-difference self-supervised pre-training for anomaly detection and segmentation. In *ECCV*, pages 392–408, 2022. 2, 3, 4